

Electronic Supplementary Information

**Engineering Au/MnO₂ hierarchical nanoarchitectures
for ethanol electrochemical valorization**

Lorenzo Bigiani,^a Teresa Andreu,^{bc} Chiara Maccato,^{*a} Ettore Fois,^d
Alberto Gasparotto,^a Cinzia Sada,^e Gloria Tabacchi,^{*d} Dileep Krishnan,^f
Johan Verbeeck,^f Juan Ramón Morante^{bc} and Davide Barreca^g

^a *Department of Chemical Sciences, Padova University and INSTM, 35131 Padova, Italy.
E-mail: chiara.maccato@unipd.it*

^b *IREC, Catalonia Institute for Energy Research, 08930 Sant Adrià de Besòs, Barcelona, Catalonia, Spain*

^c *Universitat de Barcelona (UB), 08028 Barcelona, Spain*

^d *Department of Science and High Technology, Insubria University and INSTM, 22100 Como, Italy. E-mail: gloria.tabacchi@uninsubria.it*

^e *Department of Physics and Astronomy, Padova University and INSTM, 35131 Padova, Italy*

^f *EMAT and NANOLab Center of Excellence, University of Antwerp, 2020 Antwerpen, Belgium*

^g *CNR-ICMATE and INSTM, Department of Chemical Sciences, Padova University, 35131 Padova, Italy*

§ S1. Experimental section

Synthesis: MnO₂ nanodeposits were grown by plasma assisted-chemical vapor deposition (PA-CVD) from electronic-grade Ar/O₂ plasmas using a home-built two-electrode plasma apparatus equipped with a 13.56 MHz radio frequency (RF) generator. Porous Ni foams (NFs; Ni-4753, RECEMAT BV; lateral size = 10 mm × 15 mm), endowed with a desirable open-pore structure providing excellent mass transport and a large surface per unit area,^{1,2} were adopted as scaffolds. Before deposition, NFs were cleaned by sonication in dichloroethane (10 min), 3.5 M HCl (10 min) and ethanol (10 min), in order to remove the surface oxide layer formed upon air exposure and other eventual undesired impurities.¹⁻⁵ In each deposition, the substrates were mounted on the grounded electrode and Mn(hfa)₂•TMEDA (Hhfa = 1,1,1,5,5,5-hexafluoro-2,4-pentanedione; TMEDA = *N,N,N',N'*-tetramethylethylenediamine)^{6,7} was used as manganese molecular precursor. After a preliminary screening of processing conditions, growth processes were performed at 300°C for a duration of 180 min at 20 W RF power and 1.0 mbar total pressure, with the inter-electrode distance fixed at 60 mm. In each experiment, the manganese precursor (0.30 g) was heated at 70°C by means of an external oil bath, and its vapors were delivered into the chamber by an Ar flow (60 standard cubic centimeters per minute (sccm)) through gas lines maintained at 130°C. Additional Ar and O₂ flows (15 and 5 sccm, respectively) were independently introduced into the reactor. Functionalization with gold nanoparticles was performed by RF-sputtering from Ar plasmas, with a gold target (BALTEC AG, 99.99%) mounted on the RF electrode and the above obtained manganese oxide systems fixed on the grounded one. Depositions were carried out for 30 min at a growth temperature of 60°C, using an Ar flow rate of 10 sccm, a total pressure of 0.3 mbar and an RF-power of 5 W. The setting of parameters enabled to prevent the complete coverage of manganese oxide nanosystems by a continuous gold overlayer.

Before characterization, all the target specimens were subjected to a thermal treatment at 500°C for 60 min in air, in order to attain a proper stabilization before electrochemical tests.

Characterization: X-ray diffraction (XRD) patterns were collected using a Bruker D8 Advance X-ray diffractometer equipped with a Göbel mirror and a CuK α X-ray source (40 kV, 40 mA) at a fixed incidence angle of 1.0°.

The system surface chemical composition was investigated by X-ray photoelectron spectroscopy (XPS). The measurements were carried out in a Perkin-Elmer Φ 5600ci system

using a non-monochromatized AlK α radiation ($h\nu = 1486.6$ eV), at a working pressure of 10^{-9} mbar. Binding energy (BE) values were corrected for charging phenomena by assigning a position of 284.8 eV to the adventitious C1s photopeak.⁸ To overcome the overlap between the Mn3s and Au4f photopeaks, the analysis was focused on the interference-free Au4d_{5/2} signal.⁸⁻¹⁰ After subtraction of a Shirley background, atomic percentages (at.%) values were obtained by photopeak integration, using standard PHI V5.4A sensitivity factors. Fittings were performed by Voigt functions using the XPS Peak 4.1 software.¹¹ Quantitative analyses yielded the following values: Au: 3.3 at.%, Mn: 34.1 at.%, O: 62.6 at.%, for Au/MnO₂; Au: 4.1 at.%, Ni: 27.8 at.%, O: 68.1 at.%, for Au/Ni foam. Correspondingly, gold molar fraction was determined as:¹²

$$X_{Au} = ((Au \text{ at.}\%) / (Au \text{ at.}\% + A \text{ at.}\%) \times 100) \quad (S1)$$

where A = Mn and Ni for Au/MnO₂ and Au/Ni foam, respectively.

In-depth secondary ion mass spectrometry (SIMS) analyses were carried out by a IMS 4f mass spectrometer (Cameca, Padova, Italy) using a 14.5 keV Cs⁺ primary ion beam (25 nA, 0.3% stability) and an electron gun for charge compensation. Negative secondary ion detection was performed in beam blanking mode and high mass resolution configuration, rastering over a 175 \times 175 μm^2 area and collecting elemental signals from a sub-region of size below 8 \times 8 μm^2 . By exploiting the SIMS imaging mode, the data acquisition was focused on the solid structure of the sponge and the depth profiling was carried out on this selected region. The erosion rate was evaluated through measurements of crater heights at various depths by means of a Tencor Alpha Step profilometer, yielding thus the conversion of sputtering time into depth. Scanning electron microscopy (SEM) measurements were performed by collecting in-lens and backscattered electrons using a Zeiss SUPRA 40VP instrument, at primary beam voltages of 10 kV. The mean aggregate dimensions were evaluated using the ImageJ[®] software.¹³

An aberration corrected FEI Titan3 transmission electron microscope operated at an acceleration voltage of 300 kV was used for high angle annular dark field-scanning transmission electron microscopy (HAADF-STEM), high resolution (HR)-TEM, selected area electron diffraction (SAED) and energy dispersive X-ray spectroscopy (EDXS) analyses. Samples for cross-sectional analysis were prepared using Ga-focused ion beam milling on a FEI Helios Nanolab 650 followed by an *in-situ* lift-out step using an omniprobe, and further fine thinning step at 8 kV and, finally, 2 kV ion beam energy, to obtain an electron transparent sample with

sub-100 nm thickness. Electron probe current values of 50 and 200 pA were used for atomic resolution HAADF-STEM imaging and EDXS chemical mapping, respectively. 512 pixels × 512 pixels maps were acquired with a dwell time of 10 μs/pixel, cumulatively for 12 min to obtain a high signal-to-noise ratio. To suppress the scan noise, when necessary, the images have been processed by applying a neural network filter.¹⁴

Electrochemical tests: Electrochemical tests were performed by a computer-controlled potentiostat (VMP3, BioLogic Science Instruments) using a three-electrode set-up (Fig. 3a). The working, counter, and reference electrodes were a Ni foam-supported specimen (≈1.5 cm² geometric area), a platinum mesh and a Hg/HgO (MMO) electrode (typically employed in alkaline media),¹⁵⁻¹⁸ respectively. The electrolyte was a 0.5 M ethanol in aqueous KOH solution (0.5 M). The potential was transformed into the reversible hydrogen electrode (RHE) scale by the relation:¹⁹

$$E_{\text{RHE}}(\text{V}) = E_{\text{MMO}}(\text{V}) + 0.0592 \times \text{pH} + 0.111 \quad (\text{S2})$$

Linear sweep voltammetry (LSV) experiments were performed using a scan rate of 1 mV/s. Tafel slopes were calculated by plotting the current-potential data in the form E vs. $\log j$. Chronoamperometry (CA) analyses were performed at a constant potential of 1.5 V (vs. RHE). The obtained currents were normalized to the above electrode area, in order to enable a direct comparison of the catalytic activity of different samples. In fact, BET measurement of surface area values for supported nanosystems like the present ones is a critical issue. In such cases conventional N₂ or Kr physisorption methods fail, due to the extremely low mass of the active material with respect to the supporting substrate. Furthermore, the peculiar material chemico-physical characteristics and the intrinsic uncertainty in the estimation of double layer capacitance and specific capacitance^{20, 21} prevent from a reliable calculation of the electrochemical active surface area (ECSA). On the basis of these issues, the material catalytic activity was related to the geometrical surface, which has indeed a practical meaning in terms of technological applications.²²

§ S2. Characterization

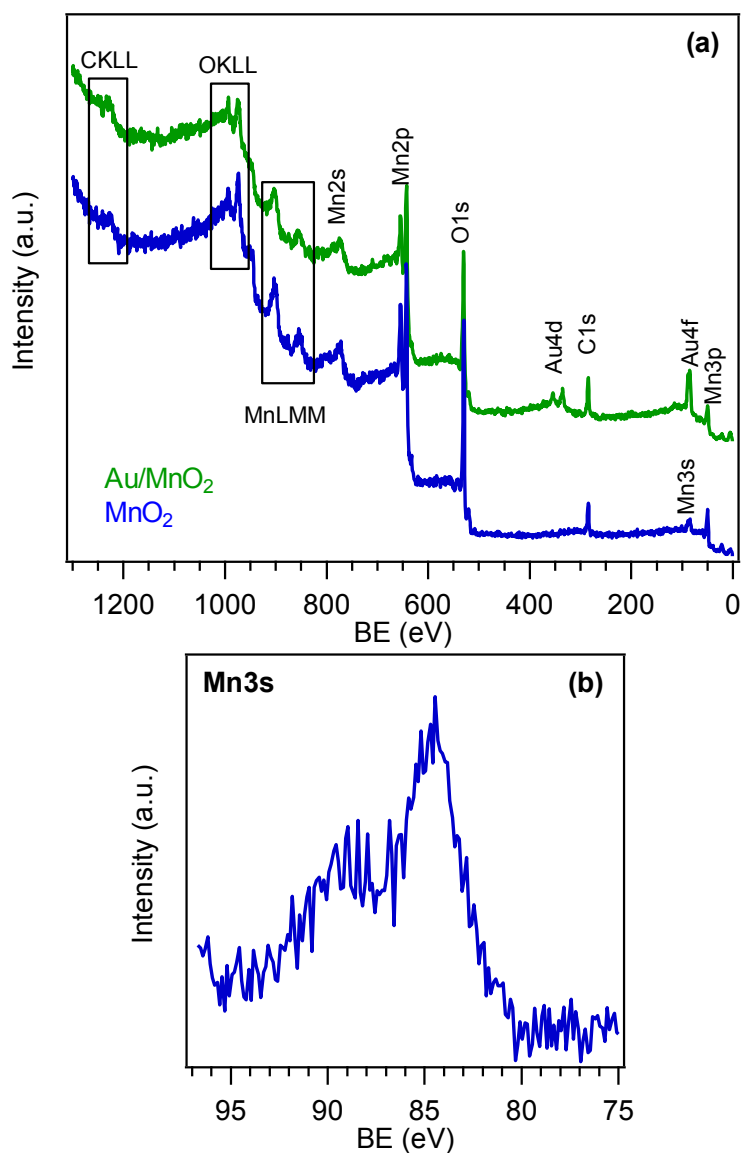


Fig. S1 Surface XPS wide-scan spectra (a) and Mn_{3s} photopeak (b) for MnO₂ and Au/MnO₂ systems. For the latter one, the Mn_{3s} peak is not displayed due to its heavy overlap with the most intense Au_{4f} signal.¹⁰

Survey spectra (Fig. S1a) were dominated by the presence of Mn and O photoelectron and Auger signals, beside the C1s signal due to air exposure, and clearly showed the presence of gold peaks after functionalization by RF-sputtering.

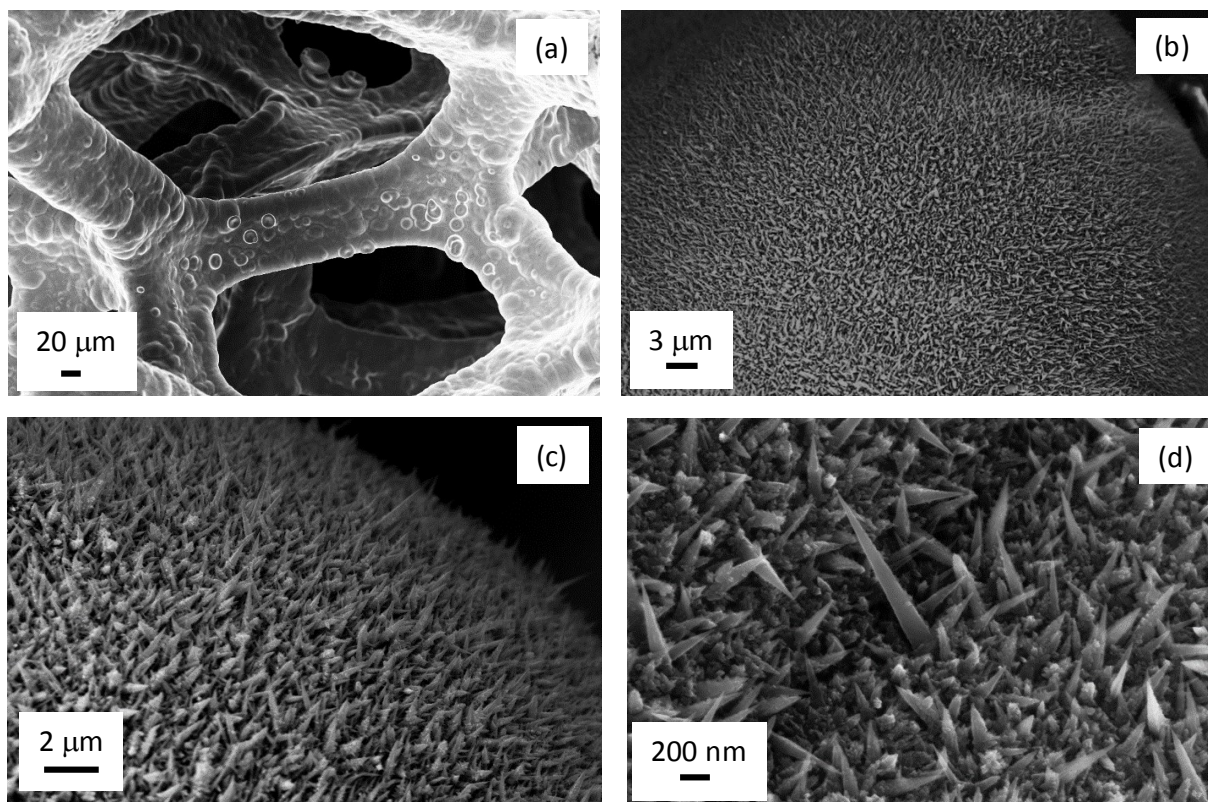


Fig. S2 FE-SEM micrographs of bare NF substrate (a) and bare MnO_2 at different magnification levels (b-d).

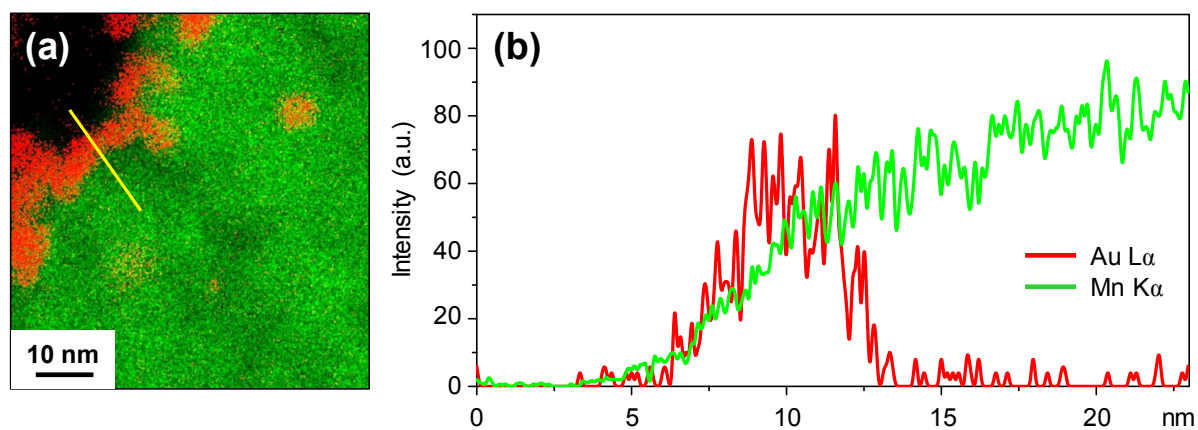


Fig. S3 (a) Representative high magnification EDXS elemental map at the Au/MnO_2 interface. (b) EDXS line-scan profiles for $\text{Au L}\alpha$ and $\text{Mn K}\alpha$, recorded along the yellow line marked in (a).

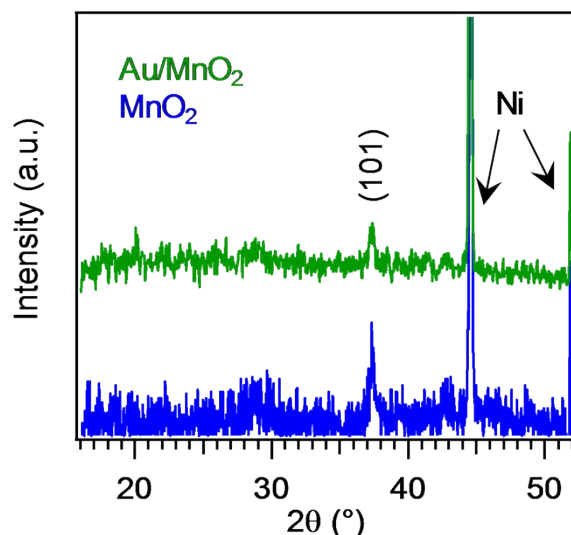


Fig. S4 XRD patterns for MnO₂ and Au/MnO₂ specimens. The signals pertaining to Ni foam substrates are marked for clarity.

XRD patterns of both bare and functionalized MnO₂ displayed only one well-detectable reflection located at $2\theta \approx 37.3^\circ$, related to the (101) crystallographic planes of tetragonal β -MnO₂, the equilibrium phase of manganese dioxide at standard temperature and pressure^{23, 24} ($P4_2/mnm$ space group; $a = 4.39 \text{ \AA}$, $c = 2.87 \text{ \AA}$).²⁵⁻²⁷ The absence of the most intense (110) peak in the reference powder spectrum, expected at $2\theta \approx 28.7^\circ$,²⁸ suggested the possible presence of preferential orientation/texturing effects, but more detailed observations were precluded by the low diffracted intensity. The latter feature and the relatively broad reflections suggested the presence of low-sized crystalline domains with a defective structure.^{29, 30}

Upon RF-sputtering of gold, the (101) peak angular position did not undergo any appreciable variation. This finding indicated that the β -MnO₂ structure was retained after functionalization with Au, in line with previous studies on MnO₂-Au materials³¹ and with the present TEM results (Fig. 2 and S5). The lowered peak intensity could be ascribed to plasma–surface interactions,³² *i.e.* bombardment of MnO₂ upon Au deposition. The lack of any appreciable reflections related to Au was ascribed to its relatively low amount and/or small crystallite dimensions, suggesting a high dispersion of gold nanoaggregates in MnO₂ deposits,⁹ in line with TEM findings.

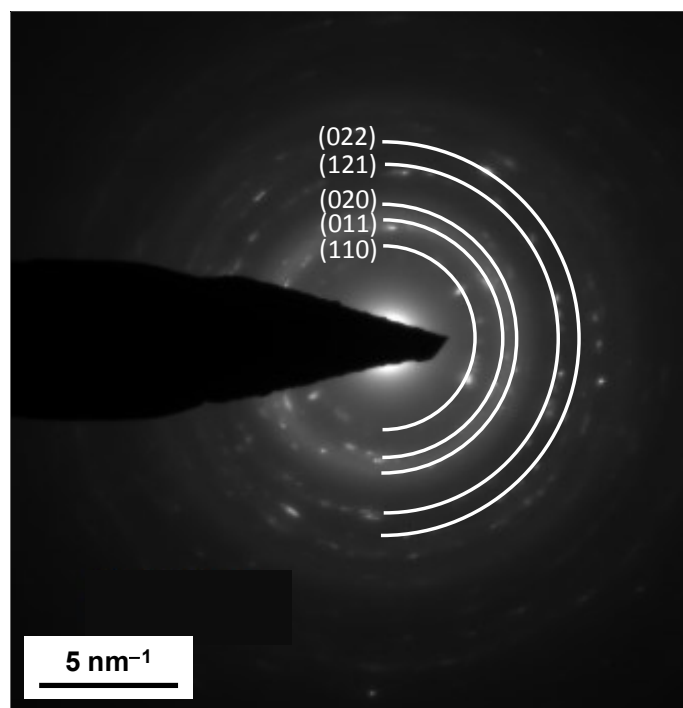


Fig. S5 SAED pattern recorded on quasi-1D MnO_2 nanoaggregates in Fig. 2g.

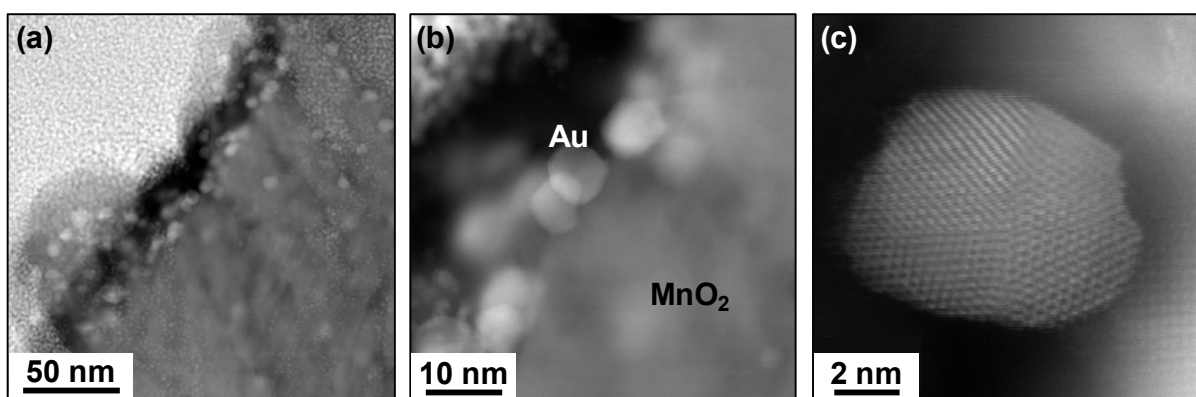


Fig. S6 (a)-(c) Representative HAADF-STEM micrographs at the Au/ MnO_2 interface from low to high magnification.

§ S3. Electrochemical tests

Materials	Onset potential @ 0.1 mA/cm ² (mV)	Potential @ 10 mA/cm ² (E _{j=10}) (V)
Au/MnO₂	41	1.41
MnO₂	109	1.44
Ni foam	118	1.45
Au/Ni foam	112	1.45

Table S1 Onset potential (voltage required to reach a current density of 0.1 mA/cm²) and E_{j=10} (voltage needed to reach 10 mA/cm²) for the target systems. The values pertaining to Ni foam, both as such and functionalized with Au NPs, are reported for comparison.

Material	j @ 1.6 V vs. RHE (mA/cm ²)	E _{j=10} (V)	[EtOH] (mol/L)	[OH ⁻] (mol/L)	Ref.
Supported films/nanosystems					
Au/MnO ₂	63	1.41	0.5	0.5	Present work
MnO ₂	44	1.44	0.5	0.5	
Ni foam	40	1.45	0.5	0.5	
Au/Ni foam	38	1.45	0.5	0.5	
PtCoPt	/	/	1.0	0.1	33
Au/TiO ₂	/	/	1.0	1.0	34
Ni/C	35	1.29	1.0	1.0	18
Ni-MgO/C	95	1.39	1.0	1.0	
Ni-Fe ₂ O ₃ /C	120	1.14	1.0	1.0	15
Ni-ZnO/C	80	1.14	1.0	1.0	
Ni-Co ₃ O ₄ /C	60	1.14	1.0	1.0	
Ni-MnO ₂ /C	50	1.14	1.0	1.0	
Ni/C	35	1.44	1.0	1.0	
Powders immobilized on substrates using slurries with additives/binders					
NiCo ₂ O ₄ /GCE	8	1.69	0.5	1.0	35
NiO/GCE	2	/	0.5	1.0	
Co ₃ O ₄ /GCE	1	/	0.5	1.0	
Co ₃ O ₄ nanosheet	100	1.45	1.0	1.0	36
Co ₃ O ₄ nanocubes	28	1.55	1.0	1.0	
ZnO/TiO ₂	0	1.74	3.0	1.0	37
MnO ₂ -vulcan	0.5	/	1.0	0.2	38
Pd-Ni/MnO ₂ /Vulcan	1	/	1.0	0.2	
Pd-Ni-Fe/MnO ₂ /Vulcan	2	/	1.0	0.2	
MnO ₂	0.4	/	1.0	1.0	16
Ni-Fe LDH	3	/	1.0	1.0	
LDH@MnO ₂	4	/	1.0	1.0	

Table S2 Comparison of EOR performances of the actual materials with selected data reported for other systems. GCE = glassy carbon electrode; LDH = layered double hydroxide. Materials which exhibited higher current density and/or lower E_{j=10} than the present MnO₂ and Au/MnO₂ specimens were operated in solutions with ethanol and KOH concentrations higher than in the present work).

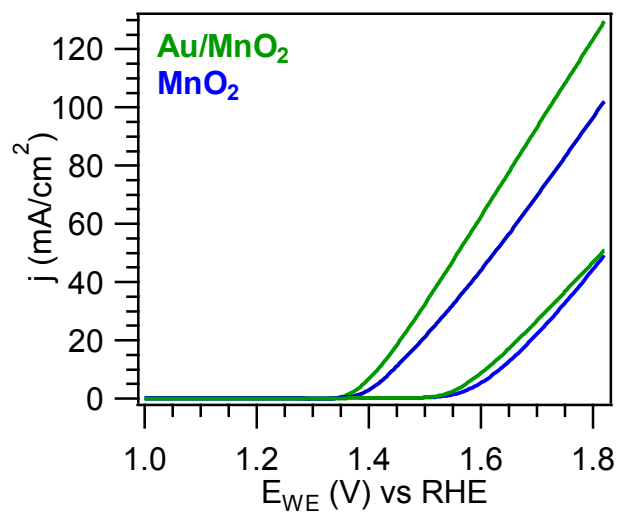


Fig. S7 Linear sweep voltammetry (LSV) curves obtained in 0.5 M KOH (dashed lines) and 0.5 M KOH + 0.5 M ethanol (continuous lines) at a scan rate of 1 mV/s.

§ S4. Computational details

General computational setup and model building: The computational *in silico* experiments were performed within the theoretical framework of the density functional theory (DFT), using the Perdew-Burke-Ernzerhof (PBE) approximation, in conjunction with dispersion corrections.^{39, 40} The interactions of valence electrons with nuclear cores were treated by means of ultra-soft pseudopotentials for all atoms.⁴¹ To compute the electronic structure, the Hubbard model was employed for Mn, with U parameter of 5 eV.^{42, 43} The wavefunctions were expanded in planewaves (PW). The PW expansion had a cutoff of 30 Ry (240 Ry for the electronic density). The sampling of the Brillouin zone was performed by selecting a 2×2×1 mesh. All the calculations were carried out with the Quantum Espresso Code.⁴⁴ Geometry optimizations of all the model systems considered in this work were performed by releasing all atoms with the exception of those of the bottom layer. The adopted convergence criterion was 0.5×10^{-3} Hartree×Bohr⁻¹.

Modeling of the MnO₂ surface: The MnO₂(101) surface was simulated using a slab model. The stoichiometry of the resulting model slab is Mn₄₈O₉₆ (for a graphical representation, see Fig. S8a). The resulting magnetization was as reported for *pyrolusite*, where the octahedral Mn sites exhibit an antiferromagnetic ordering. The exposed surface is perpendicular to the z direction and its area is 10.5 Å×13.2 Å = 1.47 nm² (the cell parameters were taken from ref.²⁸). A vacuum region of 15 Å was employed to reduce the inter-slab interactions along the z direction.

Modeling of the MnO₂-Au surface: The decorated oxide surface was built by adding on the MnO₂ model slab an Au₁₂ cluster to one of the two free surfaces of the slab. Geometry optimization of the decorated surface was then performed, yielding the structure depicted in Fig. S8b.

Modeling of ethanol adsorption on the MnO₂ surface: An ethanol molecule (EtOH) was positioned on the top of the optimized MnO₂ slab. The geometry of this new model (simulation cell stoichiometry: Mn₄₈O₉₆·EtOH) was subsequently optimized (see Fig. S9a).

Modeling of ethanol adsorption on the MnO₂-Au surface: An ethanol molecule was positioned on the top of the MnO₂-Au slab, and the geometry of the resulting model (Au₁₂Mn₄₈O₉₆·EtOH) was then optimized (Fig. S9b).

The binding energy (BE) of ethanol on the MnO₂ and MnO₂-Au surfaces was calculated using

the following formula:

$$BE = -[E(\text{EtOH}/\text{surface}) - E(\text{surface}) - E(\text{EtOH})] \quad (\text{S2})$$

where $E(\text{EtOH}/\text{surface})$ is the total energy of the slab model (either MnO_2 or $\text{MnO}_2\text{-Au}$) with adsorbed ethanol, $E(\text{surface})$ is the total energy of the slab model (either MnO_2 or $\text{MnO}_2\text{-Au}$) without ethanol, and $E(\text{EtOH})$ is the total energy of an isolated ethanol molecule. Positive values of the binding energy denote a favorable interaction of ethanol with the surface.

Bader charge analysis: Bader charges^{45, 46} were computed from the valence electronic density obtained from a single point calculation on the optimized geometries using Projector Augmented Wave (PAW) pseudopotentials.⁴⁷ In this case, the wavefunction and electron density cutoff were 40 Ry, and 400 Ry, respectively. Even the PAW calculations were performed with the PWscf module of the Quantum espresso code.⁴⁴ A dense grid was selected for representing the electronic density, giving an accuracy of ± 0.005 electrons. Atomic Bader charges and volumes were computed using Henkelman's Bader code.⁴⁸⁻⁵¹

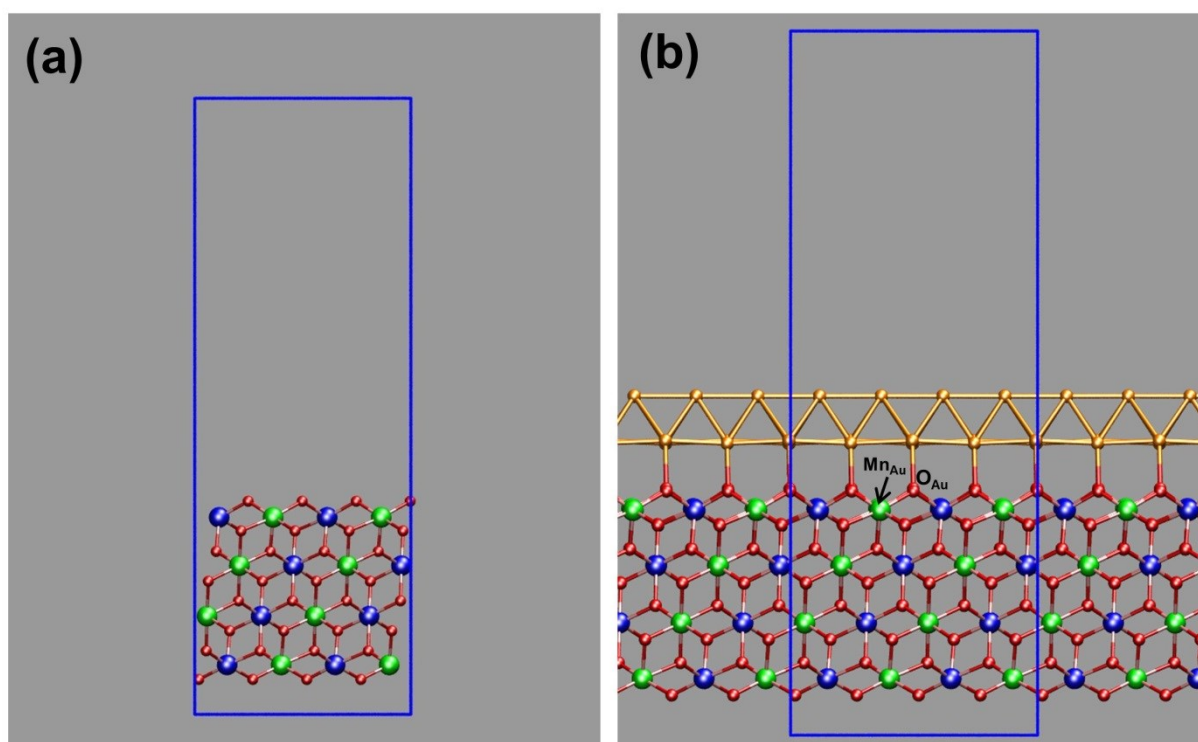


Fig. S8 (a) Graphical representation of the simulation cell content of the bare $\text{MnO}_2(101)$ slab (simulation cell stoichiometry: $\text{Mn}_{48}\text{O}_{96}$). (b) Graphical representation of the (periodically repeated) simulation cell of the $\text{Au}/\text{MnO}_2(101)$ slab (simulation cell stoichiometry: $\text{Au}_{12}\text{Mn}_{48}\text{O}_{96}$). Both (a) and (b) slab models exhibit an antiferromagnetic ordering of the Mn sites. Atom color codes: Blue spheres: Mn (spin-up); Green spheres: Mn (spin-down); Red spheres: O; Gold spheres: Au. The blue solid lines are a guide for the eye which indicate the simulation box, with periodic boundary conditions (pbc). Atom labels as in text and Tables S3-S4.

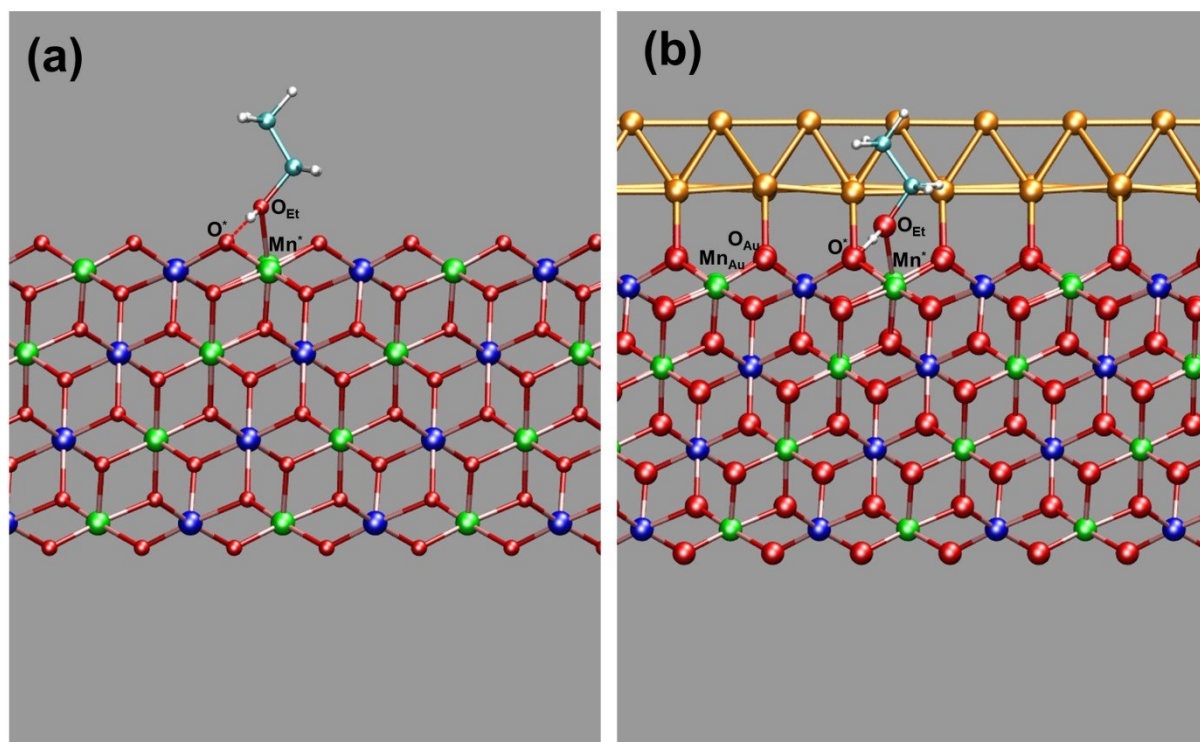


Fig. S9 (a) Graphical representation of the bare MnO₂(101) slab with an adsorbed ethanol (EtOH) molecule (simulation cell stoichiometry: Mn₄₈O₉₆·EtOH). (b) Graphical representation of the Au/MnO₂(101) slab with an adsorbed ethanol molecule (simulation cell stoichiometry: Au₁₂Mn₄₈O₉₆·EtOH). Both models exhibit an antiferromagnetic ordering of the Mn sites. Atom color codes: Blue spheres: Mn (spin-up); Green spheres: Mn (spin-down); Red spheres: O; Gold spheres: Au; Cyan spheres: C; White spheres: H. Atom labels as in text and Tables S3-S4.

§ S5. Supporting computational results

The MnO₂-Au optimized structure (Fig. S8b) is characterized by rather short Au-O_{Au} bonding distances, averaging to 2.16 Å. Specifically, the eight Au-O_{Au} distances may be divided into two groups of 4 distances, whose average values are 2.12 Å and 2.21 Å respectively. These distances are shorter than the sum of the respective van der Waals radii, indicating a strong interaction of the surface oxygens of the MnO₂(101) facets with Au.

The binding energies of ethanol on the MnO₂ and MnO₂-Au surfaces, as well as significant geometrical parameters are reported in Table S3. Significantly, on both surfaces, the hydroxyl oxygen of ethanol is bonded to a surface Mn cation positioned in the proximity of the Au nanostructure, labeled as Mn*. The ethanol hydroxyl oxygen O_{Et} is at 2.00 Å from Mn*, to be compared with a distance of 2.02 Å found for the MnO₂-Au case. In both cases, the ethanol hydroxyl proton is hydrogen bonded to a surface oxygen, labeled as O* (see Table S3). The hydrogen bond becomes particularly strong when the EtOH molecule is adsorbed on the MnO₂-Au surface (see Table S3). Both the C-O and O-H bonds of ethanol are appreciably elongated with respect to isolated EtOH - especially when the molecule is adsorbed on MnO₂-Au, while the C-C bond distance does not undergo significant changes.

	MnO ₂ -EtOH	MnO ₂ -Au-EtOH	Isolated EtOH
BE (kcal/mol)	26.7	21.2	-
O_{Et}-H (Å)	1.04	1.08	0.98
C-O_{Et} (Å)	1.46	1.45	1.44
C-C	1.52	1.52	1.52
O*-H (Å)	1.52	1.37	-
Mn*-O_{Et} (Å)	2.00	2.02	-

Table S3 Binding energy and geometrical parameters of EtOH on MnO₂ and MnO₂-Au. Atom labels as in Fig. S9.

To establish if the decoration of the MnO₂ surface with Au may lead to charge transfer at the metal/oxide interfaces, we performed a Bader charge analysis of the slab models in the framework of the Quantum Theory of Atoms In Molecules (QTAIM).^{45, 46}

Bader charges calculated for the atoms constituting the slab models used in this study were computed and averaged over all atoms of the same kind in each model in order to gather information on the partial charge located on average on the O, Mn, and Au atoms of the slab. These data are reported in Table S4. Averages were also calculated over specific groups of atoms – for example, over the eight O atoms directly coordinated to the Au atoms of the Au/MnO₂ slab, labeled as O_{Au} (the average charge computed for the same O atoms on the bare slab, in the absence of Au, is also reported for comparison in Table S4).

Atom charge ^a	MnO ₂	MnO ₂ -Au	MnO ₂ -EtOH	MnO ₂ -Au-EtOH
Average O	-0.95	-0.96	-0.95	-0.96
Average Mn	+1.90	+1.89	+1.90	+1.89
Average Au	-	+0.13	-	+0.13
Average Au_O^b	-	+0.20	-	+0.20
Average O_{Au}	-0.89	-0.96	-0.89	-0.95
Average Mn_{Au}	+1.87	+1.77	+1.87	+1.78

Table S4 Average Bader charges for the surface atoms of the four model slabs. ^a Bader charges are in electronic charge unit. ^b Au_O are the Au atoms directly in contact with surface oxygens. Other atom labels as in Fig. S8b and S9.

First of all, the data in Table S4 indicate that, in presence of Au, a charge transfer occurs from the metal nanostructure to the MnO₂ surface. Overall, each Au atom in direct contact to the surface donates on average 0.2 electrons to the surface, whereas the Au atoms not in contact with the surface remain neutral (their Bader charge is zero). Hence, charge injection occurs essentially from the Au atoms coordinated to the surface oxygens. On average, this charge donation equally affects the O and Mn atoms of the slab, which acquire 0.01 electron each. However, the Mn cations closest to the noble metal (labeled Mn_{Au} in Fig. S8b and S9b) are, individually, the most affected by the electron transfer: in passing from the bare to the decorated surface, each Mn_{Au} gains on average 0.1 electrons. This indicates that, on a local level, the donated charge concentrates mainly on the Mn atoms bonded to the oxygen atoms directly coordinated to Au (labeled as Mn_{Au}). Since the portion of electronic charge transferred by Au to the generic Mn surface atoms is much lower than that donated to the nearest

neighbor Mn atoms Mn_{Au} (0.01e vs. 0.1e), its effect should likely be unappreciable at the length scales of the surface areas typically sampled during XPS measurements. Hence, these computational data would explain why no appreciable variation of the Mn2p BE could be observed upon going from bare MnO_2 to Au/MnO_2 (Figure 1b, main text).

This picture remains unaltered in passing to the models with an adsorbed EtOH molecule (see Table S4).

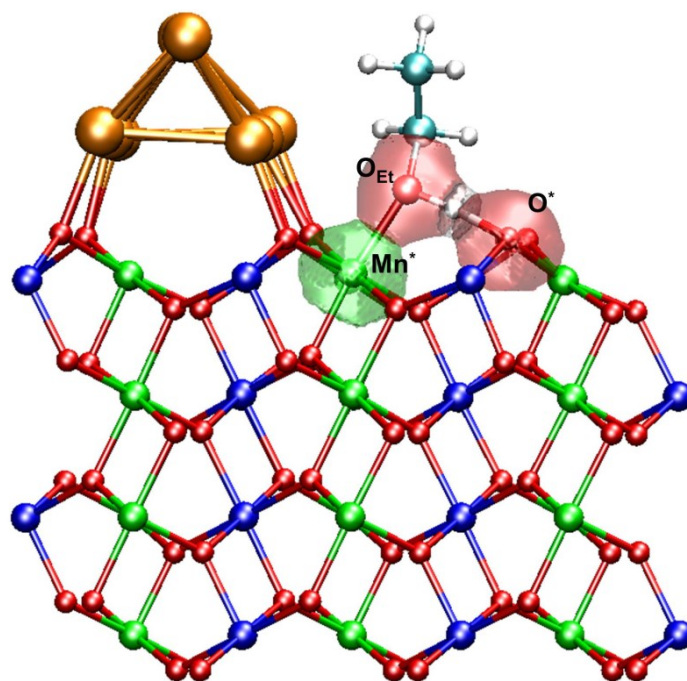


Fig. S10 Graphical representation of the Au-decorated $MnO_2(101)$ slab with an adsorbed ethanol molecule. The Bader volumes associated to the O and H atoms of ethanol and to the Mn^* and O^* atoms of the surface are represented as shaded regions (Red=oxygen; White = hydrogen; Green= Mn^*) (isodensity contour used for the picture = $0.04 e/\text{\AA}^3$). Atom color codes: Blue spheres: Mn (spin-up); Green spheres: Mn (spin-down); Red spheres: O; Gold spheres: Au; Cyan spheres: C; White spheres: H.

The partially covalent character of the EtOH-surface hydrogen bond can be visually represented by the Bader volumes associated to the hydroxyl proton, the MnO_2 surface oxygen involved in the hydrogen bond (O^*) and the hydroxyl oxygen of ethanol O_{Et} (Fig. S10). The QTAIM states that each Bader volume (also known as *atomic basin*) encloses a single maximum of the electron density. Moreover, each Bader volume is delimited by a zero-flux surface of the electron density, - *i.e.* the electron density gradient component normal to this surface is zero. Such zero-flux surfaces partition the molecular electronic density into distinct atomic basins and are characteristic of bonding interactions.⁵² As depicted in Fig. S10, the atomic basin associated to the hydroxyl proton has a common zero-flux surface of the electron

density with both the neighboring oxygen atoms, thus underlining the electronic coupling of the proton with both ethanol and the oxide surface. The Bader volumes associated to the ethanol hydroxyl oxygen and to the Mn* surface atom, respectively represented as red and green shaded regions in Fig. S10, also have a common surface, indicating that also this interaction has an appreciable covalent character.

References

1. F. Urbain, R. Du, P. Tang, V. Smirnov, T. Andreu, F. Finger, N. Jimenez Divins, J. Llorca, J. Arbiol, A. Cabot and J. R. Morante, *Appl. Catal. B*, 2019, **259**, 118055.
2. C. Xiao, S. Li, X. Zhang and D. R. MacFarlane, *J. Mater. Chem. A*, 2017, **5**, 7825-7832.
3. D. Zhang, J. Zhang, H. Wang, C. Cui, W. Jiao, J. Gao and Y. Liu, *J. Alloys Compd.*, 2019, **806**, 1419-1429.
4. N. K. Chaudhari, H. Jin, B. Kim and K. Lee, *Nanoscale*, 2017, **9**, 12231-12247.
5. Z. Li, M. Shao, H. An, Z. Wang, S. Xu, M. Wei, D. G. Evans and X. Duan, *Chem. Sci.*, 2015, **6**, 6624-6631.
6. D. Barreca, G. Carraro, E. Fois, A. Gasparotto, F. Gri, R. Seraglia, M. Wilken, A. Venzo, A. Devi, G. Tabacchi and C. Maccato, *J. Phys. Chem. C*, 2018, **122**, 1367-1375.
7. C. Maccato, L. Bigiani, G. Carraro, A. Gasparotto, R. Seraglia, J. Kim, A. Devi, G. Tabacchi, E. Fois, G. Pace, V. Di Noto and D. Barreca, *Chem. Eur. J.*, 2017, **23**, 17954-17963.
8. D. Briggs and M. P. Seah, *Practical Surface Analysis: Auger and X-ray Photoelectron Spectroscopy*, John Wiley & Sons: New York, 2nd ed., 1990.
9. D. Barreca, L. Bigiani, M. Monai, G. Carraro, A. Gasparotto, C. Sada, S. Martí-Sánchez, A. Grau-Carbonell, J. Arbiol, C. Maccato and P. Fornasiero, *Langmuir*, 2018, **34**, 4568-4574.
10. L. Bigiani, D. Barreca, A. Gasparotto and C. Maccato, *Surf. Sci. Spectra*, 2018, **25**, 014003.
11. <https://xpspeak.software.informer.com/4.1/>.
12. G. Carraro, C. Maccato, A. Gasparotto, K. Kaunisto, C. Sada and D. Barreca, *Plasma Processes Polym.*, 2016, **13**, 191-200.
13. <http://imagej.nih.gov/ij/>.
14. T. Altantzis, I. Lobato, A. De Backer, A. Béché, Y. Zhang, S. Basak, M. Porcu, Q. Xu, A. Sánchez-Iglesias, L. M. Liz-Marzán, G. Van Tendeloo, S. Van Aert and S. Bals, *Nano Lett.*, 2019, **19**, 477-481.
15. H. B. Hassan and R. H. Tammam, *Solid State Ionics*, 2018, **320**, 325-338.
16. Z. Jia, Y. Wang and T. Qi, *RSC Adv.*, 2015, **5**, 83314-83319.
17. S. Sarkar, R. Jana, H. Vadlamani, S. Ramani, D. Mumbaraddi and S. C. Peter, *ACS Appl. Mater. Interfaces*, 2017, **9**, 15373-15382.
18. H. B. Hassan, Z. A. Hamid and R. M. El-Sherif, *Chin. J. Catal.*, 2016, **37**, 616-627.

19. S. Lian, M. P. Browne, C. Domínguez, S. N. Stamatina, H. Nolan, G. S. Duesberg, M. E. G. Lyons, E. Fonda and P. E. Colavita, *Sustain. Energy Fuels*, 2017, **1**, 780-788.
20. C. C. L. McCrory, S. Jung, J. C. Peters and T. F. Jaramillo, *J. Am. Chem. Soc.*, 2013, **135**, 16977-16987.
21. P. Connor, J. Schuch, B. Kaiser and W. Jaegermann, *Z. Phys. Chem.*, 2020, **234**, 979.
22. Q. Simon, D. Barreca, D. Bekermann, A. Gasparotto, C. Maccato, E. Comini, V. Gombac, P. Fornasiero, O. I. Lebedev, S. Turner, A. Devi, R. A. Fischer and G. Van Tendeloo, *Int. J. Hydrogen Energy*, 2011, **36**, 15527-15537.
23. S. Islam, M. H. Alfaruqi, V. Mathew, J. Song, S. Kim, S. Kim, J. Jo, J. P. Baboo, D. T. Pham, D. Y. Putro, Y.-K. Sun and J. Kim, *J. Mater. Chem. A*, 2017, **5**, 23299-23309.
24. F. Cheng, T. Zhang, Y. Zhang, J. Du, X. Han and J. Chen, *Angew. Chem. Int. Ed.*, 2013, **52**, 2474-2477; *Angew. Chem.* **2013**, 2125, 2534-2537.
25. J. F. Wang, L. J. Deng, G. Zhu, L. P. Kang, Z. B. Lei and Z. H. Liu, *CrystEngComm*, 2013, **15**, 6682-6689.
26. X. P. Li, J. Liu, Y. H. Zhao, H. J. Zhang, F. P. Du, C. Lin, T. J. Zhao and Y. H. Sun, *ChemCatChem*, 2015, **7**, 1848-1856.
27. D. Y. Li, J. Yang, W. X. Tang, X. F. Wu, L. Q. Wei and Y. F. Chen, *RSC Adv.*, 2014, **4**, 26796-26803.
28. Pattern N° 024-0735, JCPDS (2000).
29. D. Barreca, F. Gri, A. Gasparotto, G. Carraro, L. Bigiani, T. Altantzis, B. Žener, U. Lavrenčič Štangar, B. Alessi, D. B. Padmanaban, D. Mariotti and C. Maccato, *Nanoscale*, 2019, **11**, 98-108.
30. M. Fekete, R. K. Hocking, S. L. Y. Chang, C. Italiano, A. F. Patti, F. Arena and L. Spiccia, *Energy Environ. Sci.*, 2013, **6**, 2222-2232.
31. C.-H. Kuo, W. Li, L. Pahalagedara, A. M. El-Sawy, D. Kriz, N. Genz, C. Guild, T. Ressler, S. L. Suib and J. He, *Angew. Chem. Int. Ed.*, 2015, **54**, 2345-2350.
32. Q. Simon, D. Barreca, A. Gasparotto, C. Maccato, T. Montini, V. Gombac, P. Fornasiero, O. I. Lebedev, S. Turner and G. Van Tendeloo, *J. Mater. Chem.*, 2012, **22**, 11739-11747.
33. A. Santasalo-Aarnio, E. Sairanen, R. M. Arán-Ais, M. C. Figueiredo, J. Hua, J. M. Feliu, J. Lehtonen, R. Karinen and T. Kallio, *J. Catal.*, 2014, **309**, 38-48.
34. Z. Xu, J. Yu and G. Liu, *Electrochem. Commun.*, 2011, **13**, 1260-1263.
35. J. Zhan, M. Cai, C. Zhang and C. Wang, *Electrochim. Acta*, 2015, **154**, 70-76.

36. L. Dai, Q. Qin, X. Zhao, C. Xu, C. Hu, S. Mo, Y. O. Wang, S. Lin, Z. Tang and N. Zheng, *ACS Cent. Sci.*, 2016, **2**, 538-544.
37. G. M. K. Tolba, N. A. M. Barakat, A. M. Bastaweesy, E. A. Ashour, W. Abdelmoez, M. H. El-Newehy, S. S. Al-Deyab and H. Y. Kim, *J. Mater. Sci. Technol.*, 2015, **31**, 97-105.
38. A. Eshghi, E. Sadati Behbahani, M. Kheirmand and M. Ghaedi, *Int. J. Hydrogen Energy*, 2019, **44**, 28194-28205.
39. J. P. Perdew, K. Burke and M. Ernzerhof, *Phys. Rev. Lett.*, 1996, **77**, 3865-3868.
40. S. Grimme, *J. Comput. Chem.*, 2006, **27**, 1787-1799.
41. D. Vanderbilt, *Phys. Rev. B*, 1990, **41**, 7892-7895.
42. M. Cococcioni and S. de Gironcoli, *Phys. Rev. B*, 2005, **71**, 035105.
43. J. S. Lim, D. Saldana-Greco and A. M. Rappe, *Phys. Rev. B*, 2016, **94**, 165151.
44. P. Giannozzi, S. Baroni, N. Bonini, M. Calandra, R. Car, C. Cavazzoni, D. Ceresoli, G. L. Chiarotti, M. Cococcioni, I. Dabo, A. Dal Corso, S. de Gironcoli, S. Fabris, G. Fratesi, R. Gebauer, U. Gerstmann, C. Gougoussis, A. Kokalj, M. Lazzeri, L. Martin-Samos, N. Marzari, F. Mauri, R. Mazzarello, S. Paolini, A. Pasquarello, L. Paulatto, C. Sbraccia, S. Scandolo, G. Sclauzero, A. P. Seitsonen, A. Smogunov, P. Umari and R. M. Wentzcovitch, *J. Phys.: Condens. Matter*, 2009, **21**, 395502.
45. R. F. W. Bader, *Chem. Rev.*, 1991, **91**, 893-928.
46. R. F. W. Bader, *Atoms in Molecules: A Quantum Theory*, Clarendon Press, 1990.
47. P. E. Blöchl, *Phys. Rev. B*, 1994, **50**, 17953-17979.
48. <http://theory.cm.utexas.edu/henkelman/code/bader>.
49. G. Henkelman, A. Arnaldsson and H. Jónsson, *Comput. Mater. Sci.*, 2006, **36**, 354-360.
50. M. Yu and D. R. Trinkle, *J. Chem. Phys.*, 2011, **134**, 064111.
51. W. Tang, E. Sanville and G. Henkelman, *J. Phys.: Condens. Matter*, 2009, **21**, 084204.
52. C. F. Matta and R. J. Boyd, *The Quantum Theory of Atoms in Molecules*, Wiley-VCH Verlag GmbH & Co., Weinheim, Germany, 2007.